Signal modeling for low-coherence height-scanning interference microscopy

Peter de Groot and Xavier Colonna de Lega

We propose a computationally efficient theoretical model for low-coherence interferometric profilers that measure surface heights by scanning the optical path difference of the interferometer. The model incorporates both geometric and spectral effects by means of an incoherent superposition of ray bundles through the interferometer spanning a range of wavelengths, incident angles, and pupil plane coordinates. This superposition sum is efficiently performed in the frequency domain, followed by a Fourier transform to generate the desired simulated interference signal. Example applications include white-light interferometry, high-numerical-aperture microscopy with a near-monochromatic light source, and interference microscopy for thickness and topography analysis of thin-film structures and other complex surface features.

OCIS codes: 120.3180, 120.3940, 120.6650, 150.6910.

1. Introduction

Low-coherence interference microscopy has grown to be the dominant optical technique for the measurement of surface profiles and roughness of small parts. Scanning the interference objective orthogonally to the surface generates an interference signal with a localized fringe contrast that removes fringe order uncertainty. In this way, a height-scanning interferometer (also called a scanning white-light or vertical-scanning interferometer) profiles discrete structures such as steps, trenches, and disconnected surface features with nanometer-level resolution over height ranges of millimeters. Evaluation techniques extend from Fourier analysis[1,2] to measurements of peak fringe contrast.[3,4]

Although most often characterized as a white-light technique, height-scanning interferometry more generally incorporates geometric effects related to an extended source and the numerical aperture (NA) of the objective.[2] With a high NA and a diffuse source image in the pupil plane, even near-monochromatic illumination provides sufficiently narrow coherence for surface metrology by use of what are commonly thought of as scanning white-light techniques. Biegen has emphasized this point by showing that a monochromatic, high-NA measurement followed by a white-light measurement provides a means of measuring the phase change on reflection of materials.[5]

In most cases in interference microscopy, both the source geometry and the spectrum contribute perceptibly to the variation in fringe contrast during the scan. Although this is well known, common theoretical treatments in the literature neglect the contribution of source geometry for simplification and treat the system as a pure white-light interferometer with a collimated beam in object space. Although conceptually adequate for low-magnification objectives, this simplification does not correspond to actual practice in microscopy.

In this paper we provide a computationally efficient mathematical framework appropriate for numerical evaluation of height-scanning interferometers. In the model, spatial and temporal coherence together play a role in shaping the interference signal. We observe important limit cases at the high-NA and white-light extremes and interesting behavior when both high NA and broad bandwidth are present simultaneously. Experimental data confirm the accuracy of the theoretical model for practical analysis of real systems.

2. Physical Model

Figure 1 illustrates the basic features of an interference microscope based on a Mirau objective—a common choice for high-NA imaging. The object has

The authors are with the Zygo Corporation, 21 Laurel Brook Road, Middlefield, Connecticut 06455-0448. P. de Groot's e-mail address is peterd@zygo.com.

Received 21 January 2004; revised manuscript received 12 April 2004; accepted 20 May 2004.

0003-6935/04/254821-10$15.00/0

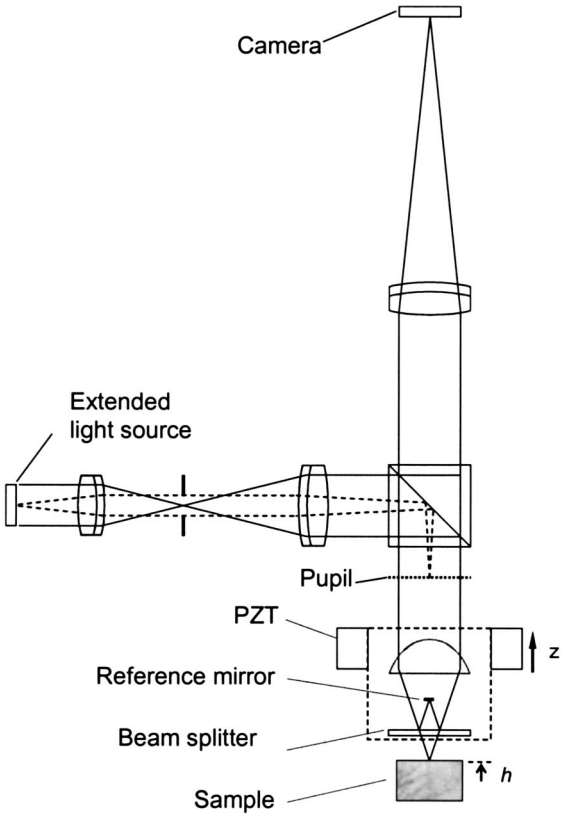

Fig. 1. Interference microscope physical model. PZT, piezoelectric transducer.

height features h that vary over the object surface. A mechanical stage provides a smooth, continuous scan ζ of the interference objective. During the scan, a computer records intensity data $I(\zeta)$ for each image point or camera pixel in successive camera frames.

A full physical model can be elaborate, taking into account the partial coherence of the light source, polarization mixing in the interferometer, the imaging properties of high-NA objectives, and the interaction of electric field vectors at high angles of incidence and in the presence of discontinuous surface features. We elect here to simplify the model by assuming a randomly polarized, low-coherence extended source and a smooth surface that does not scatter or diffract incident light. The total signal is the incoherent sum of the interference contributions of all the ray bundles passing through the pupil plane of the objective and reflecting from the object surface at an incident angle ψ, as shown in Fig. 2. A similar starting point has precedence in the literature, including papers by Davidson *et al.*,[6] Kino and Chim[7] and Sheppard and Larkin.[8]

3. Interference Signal

Following the usual two-beam interference analysis, the interference contribution for a single ray bundle through the optical system is proportional to

$$g(\beta, k, \zeta) = R + Z + 2\sqrt{RZ}\cos[2\beta k(h - \zeta) + (\upsilon - \omega)], \quad (1)$$

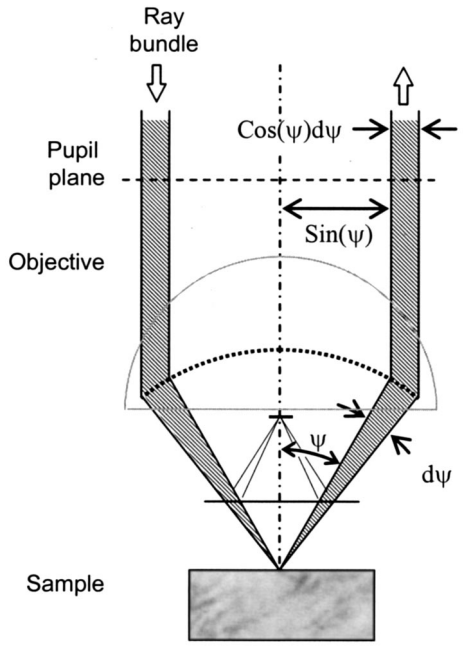

Fig. 2. Geometry of a single ray bundle illumination and imaging through an objective obeying the sine condition. The focal length is normalized.

where Z is the effective object intensity reflectivity, including, e.g., the transmissivity of the beam splitter, R is the effective reference reflectivity, including both the beam splitter and the reference mirror; and we assume a refractive index of 1 for the ambient medium. The directional cosine β for an incident angle ψ is

$$\beta = \cos(\psi), \quad (2)$$

and the angular wave number k for a source wavelength λ is

$$k = (2\pi/\lambda). \quad (3)$$

The phase term in Eq (1) has a contribution ω for the object path in the interferometer, including any phase change on reflection from the object surface, and a contribution υ for the reference path, including the reference mirror and other optics in the objective. In the general case, Z, R, υ, and ω all vary with directional cosine β and angular wave number k.

The total interference signal for a single scan position ζ is the integral over all points in the pupil plane and over all wavelengths for the ray bundle contributions $g(\beta, k, \zeta)$:

$$I(\zeta) = \int_0^\infty \int_0^1 g(\beta, k, \zeta) U(\beta) V(k) \beta \mathrm{d}\beta \mathrm{d}k, \quad (4)$$

where $U(\beta)$ is the intensity distribution in the pupil plane of the objective and $V(k)$ is the optical spectrum distribution. The extra weighting factor β in Eq. (4) follows from a $\cos(\psi)$ term attributable to the projec-

tion angle and a $\sin(\psi)$ term for the diameter of the annulus of width $d\psi$ in the pupil plane:

$$\cos(\psi)\sin(\psi)d\psi = -\beta d\beta. \quad (5)$$

We assume that the objective obeys the Abbe sine condition as shown in Fig. 2.

Certain simplifying assumptions often permit direct evaluation of Eq. (4). The most common simplification is to assume a point source in the center of the pupil plane ($U = 0$ for $\beta \neq 1$), equivalent to a low NA illumination, and a Gaussian spectrum. In the more general case of an extended source and a more complicated source spectrum, Eq. (4) implies a numerical integration. This general numerical calculation can be intensive and time-consuming. For example, use of 64 values each for both k and β and a range of 256 individual scan positions ζ, a numerical evaluation requires over 10^6 calculations of the integrand of Eq. (4) for each pixel. If we wish to simulate signals for an entire 1000×1000 pixel image, 1^{12} calculations are involved, which by any measure is a significant computational burden.

A first goal therefore of the modeling task is to derive a more computationally efficient way of simulating the interference intensity signal $I(\zeta)$.

4. Simplification by Frequency Analysis

For most applications of interest in common height-scanning interferometric microscopes, the most rapidly varying factor in the integrand of Eq. (4) as a function of k and β is the quasi-periodic interference contribution $g(\beta, k, \zeta)$. This factor in turn is modulated most rapidly by the product $2\beta k$ in the phase term, which we can redefine physically as the spatial frequency $\hat{\kappa}$ of the interference contribution $g(\beta, k, \zeta)$ that we generate by scanning orthogonally to the sample surface:

$$\hat{\kappa} = 2\beta k. \quad (6)$$

This spatial frequency $\hat{\kappa}$ is the angular rate of change of the phase term of $g(\beta, k, \zeta)$ as a function of the scan coordinate ζ. In the integration, various combinations of β and k result in the same spatial frequency $\hat{\kappa}$. One way to simplify Eq. (4) therefore is to recast the calculation in terms equivalent to these spatial frequencies. As we now show, the numerical calculation of the intensity signal $I(\zeta)$ can then be more efficiently expressed as a fast Fourier transform of the frequency-domain spectrum $q(K)$ of the signal, where K is the frequency coordinate of the transformed data.

The first step to simplify the analysis is the somewhat counterintuitive step of Fourier transforming Eq. (4), leading to a triple integral that defines $q(K)$:

$$q(K) = \int_0^\infty \int_0^1 U(\beta)V(k) \times \left[\int_{-\infty}^{\infty} g(\beta, k, \zeta)\exp(iK\zeta)d\zeta\right]\beta d\beta dk. \quad (7)$$

After expansion of the cosine term in $g(\beta, k, \zeta)$ in the usual way,

$$2\cos(\hat{\kappa}\zeta + \cdots) = \exp(i\hat{\kappa}\zeta + \cdots) + \exp(-i\hat{\kappa}\zeta - \cdots), \quad (8)$$

and using the Dirac delta function,

$$\delta(K \pm \hat{\kappa}) = \int_{-\infty}^{\infty} \exp[(K \pm \hat{\kappa})i\zeta]d\zeta, \quad (9)$$

the inner integral over ζ evaluates to

$$\int_{-\infty}^{\infty} g(\beta, k, \zeta)\exp(iK\zeta)d\zeta = \delta(K)(R + Z) + \delta(K - \hat{\kappa})\sqrt{RZ}\exp[i\hat{\kappa}h + i(\upsilon - \omega)] + \delta(K + \hat{\kappa})\sqrt{RZ}\exp[-i\hat{\kappa}h - i(\upsilon - \omega)]. \quad (10)$$

The δ functions underscore that the mathematically general frequencies K of the Fourier decomposition relate to the spatial frequency $\hat{\kappa}$ defined by Eq. (6). A logical change of variables in Eq. (7) for the second inner integral at constant k is therefore

$$\beta = \hat{\kappa}/2k, \quad (11)$$

$$d\beta = d\hat{\kappa}/2k. \quad (12)$$

After we use Eq. (10), Eq. (7) becomes

$$q(K) = \int_0^\infty \int_0^{2k} \delta(K)(R + Z)\Gamma d\hat{\kappa}dk + \int_0^\infty \int_0^{2k} \delta(K - \hat{\kappa})\sqrt{RZ}\exp[i\hat{\kappa}h + i(\upsilon - \omega)]\Gamma d\hat{\kappa}dk + \int_0^\infty \int_0^{2k} \delta(K + \hat{\kappa})\sqrt{RZ} \times \exp[-i\hat{\kappa}h - i(\upsilon - \omega)]\Gamma d\hat{\kappa}dk, \quad (13)$$

where we gathered the weighting terms as

$$\Gamma(\hat{\kappa}, k) = U[\beta(\hat{\kappa}, k)]V(k)\hat{\kappa}/4k^2. \quad (14)$$

Although for compactness we did not note the dependencies explicitly in Eq. (13), it is understood that Z, R, υ, ω, and Γ all vary with spatial frequency $\hat{\kappa}$ and wavelength k.

The presence of Dirac functions in the integrands of Eq. (13) implies that further symbolic analysis is

called for, eventually leading to the following simplification (see Appendix A):

$$q(K) = \delta(K)\int_0^\infty\int_{\kappa/2}^\infty (R + Z)\Gamma \mathrm{d}k\mathrm{d}\hat{\kappa} + H(K)\exp(iKh)\int_{K/2}^\infty \{\sqrt{RZ}\exp[i(\upsilon - \omega)]\Gamma\}_{\hat{\kappa}=+K}\mathrm{d}k + H(-K)\exp(-iKh) \times \int_{-K/2}^\infty \{\sqrt{RZ}\exp[-i(\upsilon - \omega)]\Gamma\}_{\hat{\kappa}=-K}\mathrm{d}k, \quad (15)$$

where H is the unitless Heaviside step function defined by

$$H(u) = \begin{cases} 0 & \text{for } u < 0 \\ 1 & \text{otherwise} \end{cases}. \quad (16)$$

The calculation of the frequency-domain representation of the interference signal has now been reduced to one double integral for the dc term ($K = 0$) and to single integrals over k for all other spatial frequencies ($K \neq 0$). This is a substantial simplification in terms of the number of numerical evaluations.

The incoherent superposition model accommodates polarization when the resulting Fourier components $q(K)$ are summed for s- and p-polarization contributions. Writing this explicitly for fully random polarization,

$$q(K) = q_s(K) + q_p(K), \quad (17)$$

where the s and p subscripts in Eq. (17) refer to Eq. (15) with all the relevant parameters calculated for the corresponding polarization state, including the sample reflectivity, the beam splitter, and so on.

The final calculation of the interference signal is now an inverse Fourier transform:

$$I(\zeta) = \int_{-\infty}^\infty q(K)\exp(-iK\zeta)\mathrm{d}K. \quad (18)$$

Although this is another integral, it can be evaluated by a numerical fast Fourier transform and is therefore of low computational burden.

5. Numerical Integrations

The advertised benefit of Eq. (15) is computational efficiency. To illustrate this, the integrals are replaced with sums as follows:

$$q_0 = \sum_{K\geq 0}\sum_{k>K/2}(R + Z)\Gamma, \quad (19)$$

$$q(K > 0) = \exp(iKh)\sum_{k>K/2}\sqrt{RZ}\exp[i(\upsilon - \omega)]\Gamma. \quad (20)$$

If the N discrete samples for $I(\zeta)$ are spaced by an increment ζ_{step}, there will be $N/2 + 1$ positive spatial frequencies starting from zero and rising to $N/2$ cycles per data trace, spaced by an increment

$$K_{\text{step}} = \frac{2\pi}{N\zeta_{\text{step}}}. \quad (21)$$

Unless the spectral bandwidth and or the range of incident angles is exceptionally large, only a fraction of the total frequency range is needed to fully characterize the signal. There are therefore only a few relevant K values for which $q(K)$ is nonzero. For example, if we acquire data at a nominal rate of eight camera frames per interference fringe, this is a spatial frequency of $N/8$ cycles per data trace in a numerical fast Fourier transform. Assuming quite safely that the source bandwidth is no greater than the nominal mean wavelength itself, there would be $< N/8$ values to calculate by use of Eq. (20). In the example following Eq. (5), if there are $N = 256$ individual scan positions, the number of relevant K values will be 32, and if we employ 64 angular wave numbers k in the numerical integration, there are 2048 calculations each for Eqs. (19) and (20), or of the order of 200× fewer complex calculations then a direct numerical evaluation of Eq. (4). Even after we factor in the cost of the inverse Fourier transform, this substantial relief in computation makes it more practical to perform full-field simulations of signals in low-coherence interferometry.

6. Limit Cases

It is worthwhile to consider the limit cases of collimated white-light (temporal coherence limit) and high-NA monochromatic illumination (spatial coherence limit). Along with verifying Eq. (13), these limit cases provide insight into the frequency-domain portrait of the interference signal.

For both of these limit cases, as a first simplifying step, let us assume that the phase contribution $(\upsilon - \omega) = 0$ for all K, k and that the reflectivities R, Z are independent of incident angle and wavelength, so that the integrals in Eq. (13) simplify to

$$q(K) = \delta(K)(R + Z)\int_0^\infty\int_{\hat{\kappa}/2}^\infty \Gamma(\hat{\kappa}, k)\mathrm{d}k\mathrm{d}\hat{\kappa} + H(K)\exp(iKh)\sqrt{RZ}\int_{K/2}^\infty \Gamma(K, k)\mathrm{d}k + H(-K)\exp(-iKh)\sqrt{RZ}\int_{-K/2}^\infty \Gamma(-K, k)\mathrm{d}k. \quad (22)$$

Now we have only to handle integrals involving the weighting factor $\Gamma(\hat{\kappa}, k)$ defined in Eq. (14).

The most familiar limit case is for collimated white light. The illumination angle for this case is $\psi = 0$, and consequently the pupil plane function is

$$U(\beta) = \delta(\beta - 1). \quad (23)$$

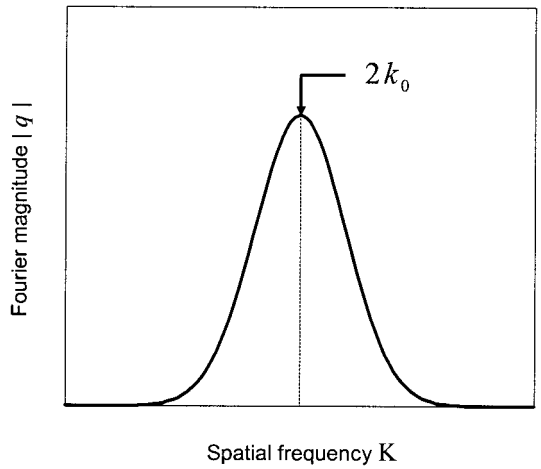

Fig. 3. Theoretical Fourier magnitude for height-scanning interferometry in the limit of a white-light source and collimated object illumination. The magnitude curve follows that of the emission spectrum of the source.

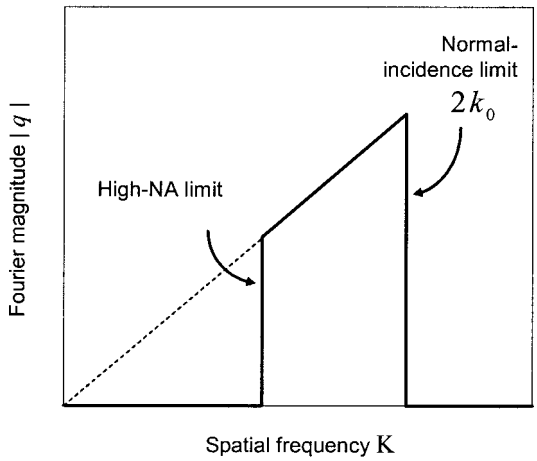

Fig. 4. Theoretical Fourier magnitude for height-scanning interferometry in the limit of a spatially incoherent, monochromatic source uniformly filling the pupil plane. The magnitude curve follows the distribution function of the pupil plane illumination, here a top hat, weighted by the spatial frequency, which is proportional to the directional cosine of the object illumination.

Rewriting in terms of k,

$$U(K, k) = \delta(K/2k - 1). \tag{24}$$

Using the mathematical identity

$$\delta[f(k)] = \frac{\delta(k - \xi)}{|\mathrm{d}f/\mathrm{d}k|_{k=\xi}}, \tag{25}$$

where ξ is the root of $f(k)$, we have

$$\Gamma(K, k) = \frac{K^2}{8}\frac{V(k)}{k^2}\,\delta(k - K/2). \tag{26}$$

The integrals simplify through the delta function to

$$\begin{aligned} q(K) = \delta(K)\frac{(R + Z)}{2}\int_0^\infty V(\hat{\kappa}/2)\mathrm{d}\hat{\kappa} \\ + H(K)\frac{\sqrt{RZ}\,\exp(iKh)}{2}V(K/2) \\ + H(-K)\frac{\sqrt{RZ}\,\exp(-iKh)}{2}V(-K/2). \end{aligned} \tag{27}$$

Looking at the positive, nonzero portion of the spectrum, we see that the magnitude of the Fourier coefficients are directly proportional to the source spectral distribution V:

$$|q(K > 0)| \propto V(k), \tag{28}$$

where, as expected, at normal incidence the frequency K is twice the angular wave number k: $k = K/2$. Relation (28) is the familiar result that there is a Fourier-transform relationship between the interference signal and the emission spectrum of the white-light source, as Fig. 3 illustrates for a Gaussian spectrum.

The opposing limit is an extended monochromatic light source. This can be represented by a delta function spectrum for a nominal angular wave number k_0:

$$V(k) = \delta(k - k_0). \tag{29}$$

Equation (22) readily simplifies to

$$\begin{aligned} q(K) = \delta(K)(R + Z)\int_0^\infty \hat{\kappa}U(\hat{\kappa}/2k_0)\mathrm{d}\hat{\kappa} \\ + H(K)H(k_0 \\ - K/2)\frac{\exp(iKh)\sqrt{RZ}}{4{k_0}^2}KU(K/2k_0) \\ + H(-K)H(k_0 + K/2) \\ \times \frac{\exp(-iKh)\sqrt{RZ}}{4{k_0}^2}KU(-K/2k_0). \end{aligned} \tag{30}$$

Looking once again at the positive, nonzero portion of the spectrum, we see that the magnitude of the Fourier coefficients are now proportional to the function U weighted by the spatial frequency K:

$$|q(K > 0)| \propto \beta U(\beta), \tag{31}$$

where the spatial frequency K is proportional to the directional cosine β: $\beta = K/2k_0$. This less familiar result reveals a Fourier-transform relationship between the interference signal and the cosine of the illumination angle, as Fig. 4 illustrates for a uniformly filled pupil.

It is interesting to compare the resulting simulated signals assuming a relative scan frequency bandwidth of $\Delta K/K = 0.2$ for both limit cases. Figure 5(a) shows the white-light limit, with a low-NA system illuminated by a broadband 100-nm Gaussian emission spectrum centered at 500 nm. Figure 5(b) shows the opposite, narrow-bandwidth case, for

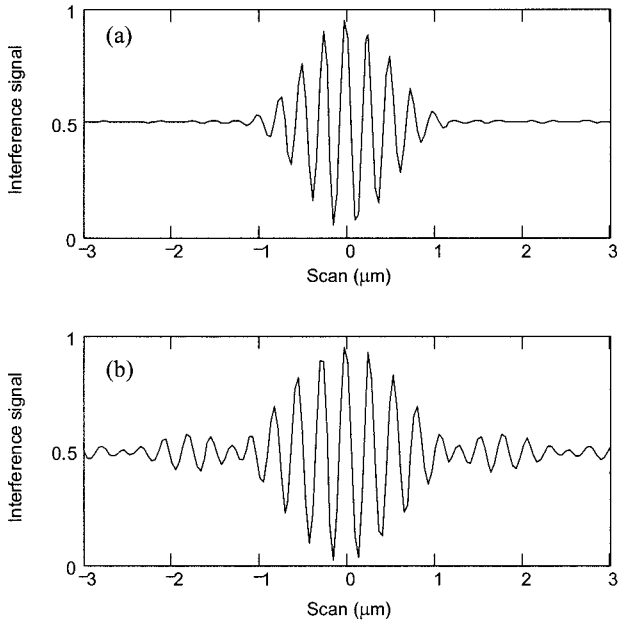

Fig. 5. Height-scanning interference signal simulations for a 500-nm light source: (a) broad 100-nm bandwidth and a more narrowly collimated 0.2-NA illumination; (b) narrow 20-nm Gaussian bandwidth and a wide, uniformly filled 0.6-NA pupil.

which the fringe contrast variation is dominated by an extended source filling a 0.6-NA pupil (directional cosine range from 0.8 to 1.0). An example of a useful application of this near-monochromatic source limit is stroboscopic interferometry, which is most effective with a laser diode or narrow-bandwidth light-emitting diode (LED) source that can be modulated at high speed.[9,10]

The plots show nearly the same coherence length for the two limit cases, with the differences between the two plots being related to the apodization of the frequency spread—the Gaussian spectrum is smoothly tapered whereas the pupil plane illumination is abruptly cut off by the NA of the system, leading to ringing. With appropriate apodization in the pupil plane, the two limit cases can be made to look nearly identical, although the high-NA case will always have a lower mean spatial frequency (with broader fringes).

7. Thin Films

Most successful interference microscope profilometry applications today are for single material surfaces. For these cases, using the Fresnel equations in the usual way,[11] one can calculate an amplitude reflectivity z that for the simplest case of an ideal beam splitter fully defines the reflectivity Z and phase shift ω for the measurement path:

$$Z(\beta, k) = |z(\beta, k)|^2, \tag{32}$$

$$\omega(\beta, k) = \arg[z(\beta, k)]. \tag{33}$$

Here again, the incoherent superposition model accommodates the dependency of the reflection coefficient z on polarization by summation of the resulting Fourier components for s- and p-polarization contributions [Eq. (17)].

A more challenging situation for an interference microscope is an object comprised of partially transparent thin-film layers. Such samples are being delivered with increasing frequency to the optical metrology laboratory as thin-film nanostructures such as microelectro mechanical system devices, flat-panel display pixels, and patterned semiconductors that extend their dominance in high-technology applications.

A straightforward example is a single-layer film deposited on a substrate. The amplitude reflectivity z becomes[12]

$$z(\beta, k) = \frac{\vartheta + \vartheta' \exp[2ikL\beta'(\beta)n']}{1 + \vartheta\vartheta' \exp[2ikL\beta'(\beta)n']}, \tag{34}$$

where L is the thickness of the film, n', is the index of the film, ϑ is the reflectivity of the air–film interface, ϑ' is the reflectivity of the film–substrate interface, and

$$\beta'(\beta) = [1 - (1 - \beta^2)/n'^2]^{1/2} \tag{35}$$

is the directional cosine of propagation within the film.

The interference signal generation for a single-layer thin film is quite interesting and has a few surprises when we consider the effects of illumination geometry. Figure 6 compares the results with various sources for a 2-μm layer of a hypothetical dielectric film of index $n' = 2$ on a substrate of index 4. Figure 6(a) shows that, with the white-light illumination, there are two distinct signals corresponding to the two interfaces. The film appears to be twice the physical thickness, the optical thickness being Ln'. The signals are well separated, and one can analyze each of them separately to determine the profile of each interface, taking into account the factor n' in translating from optical to physical thickness.[13,14] Figure 6(b) shows that, for monochromatic light and a high-NA objective, there are again two signals, but this time they are much closer together than in Fig. 6(a). Here the apparent thickness is actually inferior to the physical thickness by approximately a factor of 2. We can understand this by likening the geometric limits on coherence to a focus effect: The best focus position appears to be shifted closer to the objective when passing into a medium of higher index.

Finally we consider both high-NA and a broad spectral bandwidth together. Figure 6(c) shows that, in the competition between spatial and temporal coherence for positioning the substrate reflection, the substrate loses. The two coherence phenomena oppose each other and there is almost no modulation left for the substrate reflection.

8. System Imperfections

Many of the most common system errors in an interference microscope can be efficiently modeled by their frequency-domain characteristics.

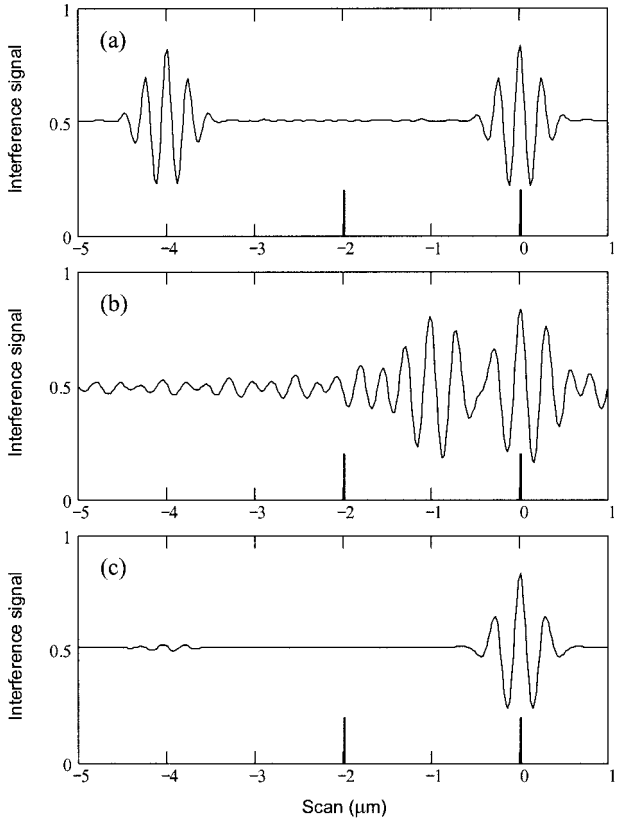

Fig. 6. Height-scanning signal simulations for a 2-μm-thick film of index 2 deposited on a substrate of index 4, viewed with a 500-nm center wavelength: (a) broad 200-nm Gaussian bandwidth, narrow 0.28-NA illumination; (b) narrow 5-nm bandwidth, wide 0.80-NA illumination; (c) both broad 200-nm bandwidth and wide 0.80-NA illumination.

As an example, a nonlinear chromatic dispersion resulting from an imbalance in refractive materials between the measurement and the reference paths can be modeled as

$$\upsilon(k) = \upsilon_0 + (k - k_0)^2 \wp, \tag{36}$$

where $\wp$ is the second-order phase dependence of υ. As illustrated in Fig. 7, this aberration leads to a broadening of the fringe contrast envelope. A similar envelope broadening for interference patterns that are limited by spatial coherence can be attributed to a nonlinear dependence of the system phase υ on the directional cosine β, which can result from optical aberrations.

Another example of a system imperfection is the signal integration time of the camera, which has the effect of averaging the signal over a range of scan positions. This often-called integrating bucket can be modeled as the convolution of a rectangular boxcar window with the signal. In the frequency domain, the convolution becomes the product of the Fourier coefficients q with a sync function.

$$B(K) = \frac{\sin(K\zeta_{\text{step}}/2)}{K\zeta_{\text{step}}/2}, \tag{37}$$

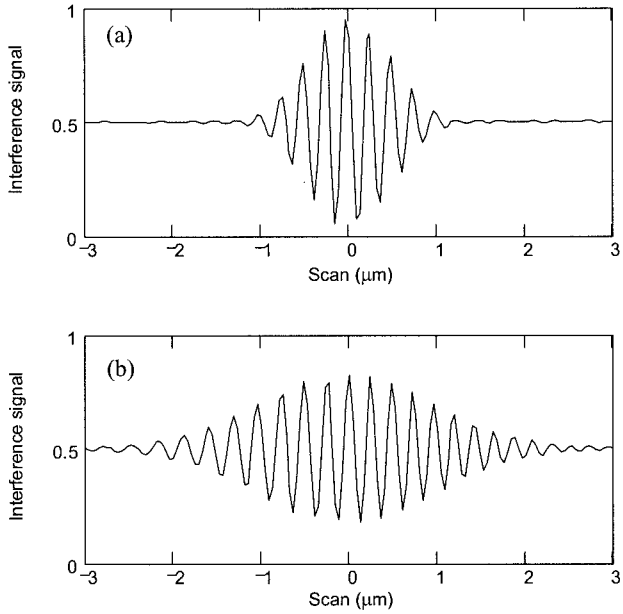

Fig. 7. Coherence broadening effect of nonlinear chromatic dispersion: (a) no dispersion, 500-nm, 100-nm bandwidth light source; (b) same source characteristics but unbalanced quadratic dispersion $\wp = 0.2\ \mu\text{m}^2$ (~0.8 fringe over the full spectrum) in the interferometer.

where ζ_{step} is the scan increment between data frames, as defined above for Eq. (21). The effect of this time integration is to dampen the contribution from the higher spatial frequencies, as well as to reduce overall fringe contrast. A similar analysis describes the spatial-frequency-dependent fringe contrast loss in a stroboscopic interferometer.[15]

Many system imperfections are field dependent. A relevant example is linear dispersion in the system phase υ, which changes the phase of the underlying carrier in the interference signal with respect to the fringe contrast envelope. The field dependence of the system phase behavior complicates the determination of fringe order.[16] Modeling this phenomenon

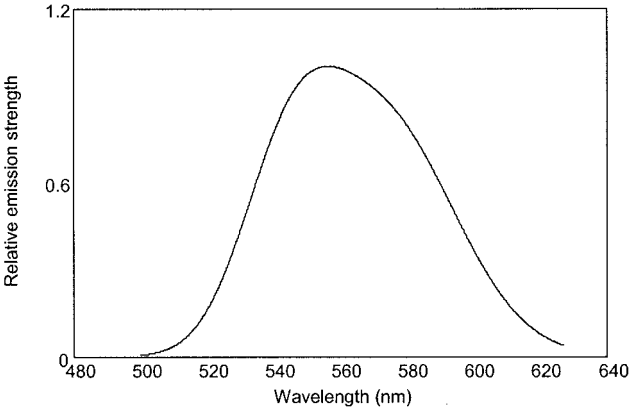

Fig. 8. Measured spectrum of a white-light LED source, nominally centered at 556 nm with a bandwidth of 62 nm, used for the experimental data acquisition in Fig. 9

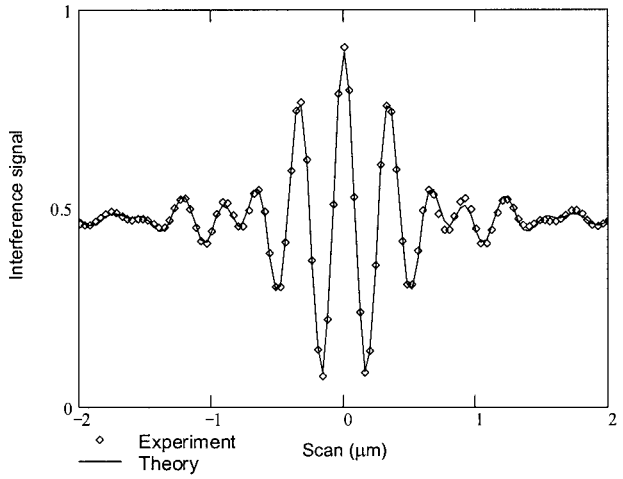

Fig. 9. Comparison of experimental and theoretical interference signals for a solid surface. The sample is a SiC optical flat, the white-light source spectrum is as in Fig. 8, and the Mirau objective has an unobscured NA range from 0.27 to 0.78.

over the full image field is an example of where computational efficiency of Eqs. (19) and (20) is a substantial benefit.

9. Experimental Verification

As a first verification of the model we view a solid-surface SiC flat using a 100×, 0.78-NA Mirau objective in a microscope with a white-light LED having the emission spectrum shown in Fig. 8. The combination of a 62-nm emission bandwidth and wide NA represents a realistic situation for which both source geometry and spectrum influence fringe localization. To keep it simple, we assume (and attempt experimentally) a uniform illumination of the pupil, thus $U(\beta) = 1$ within the NA of the objective and outside the central Mirau obscuration and is zero elsewhere.

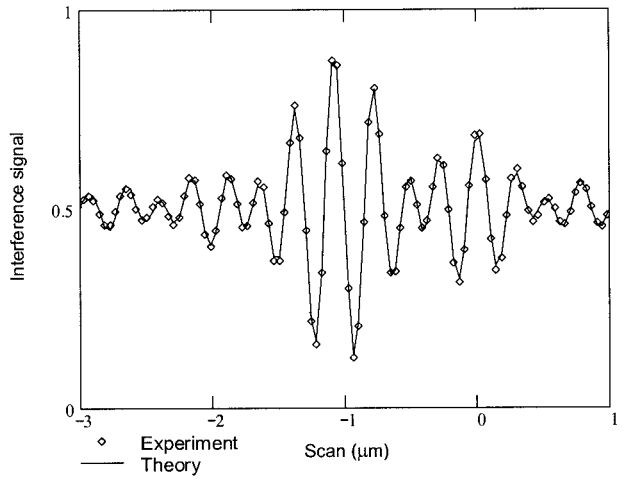

Fig. 10. Comparison of experimental and theoretical interference signals for a thin-film sample. The sample is 1025 nm of SiO_2 (index 1.45 on Si, the 498-nm LED source has an approximately Gaussian spectral bandwidth of 27 nm, and the Mirau objective has an unobscured NA range from 0.27 to 0.78.

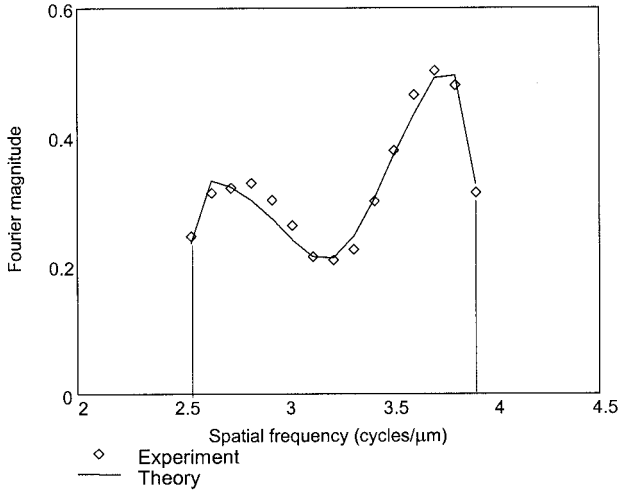

Fig. 11. Comparison of the experimental and theoretical Fourier spectrum magnitudes for the thin-film sample signal shown in Fig. 10.

We treat the interference objective as having a perfect 50/50 beam splitter with a fixed value for the reference path phase shift υ, and we allow the signal strength and an average value of the phase offset ω to be adjustable parameters in comparing experiment to theory. Figure 9 shows excellent agreement with experimental data, indicating that the simple incoherent superposition model is sufficient to simulate the main features of interference signals in practical applications.

For a thin-film example, we elect the same 100×, 0.78-NA Mirau objective as for Fig. 9 but exchange the light source for a narrow 27-nm bandwidth LED centered at 498 nm. Once again we can observe in Fig. 10 a satisfying agreement between experiment and theory. The results are so close that the difference is difficult to quantify by inspection of the signal itself. A comparison in the frequency domain, however, is more revealing. Figures 11 and 12 show

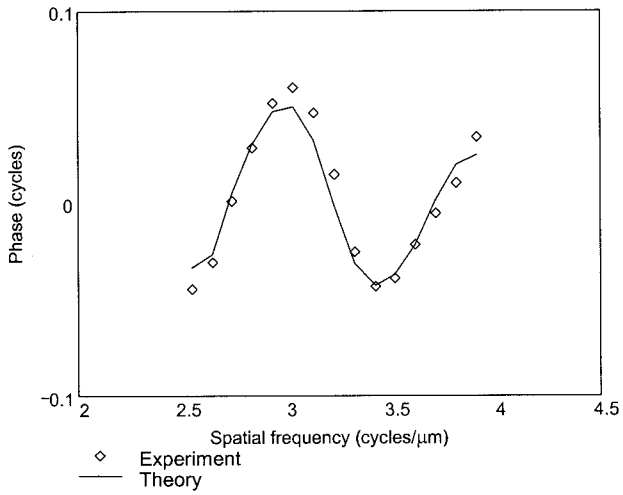

Fig. 12. Comparison of the experimental and theoretical Fourier spectrum phases for the thin-film sample signal shown in Fig. 10.

important characteristic features of thin films, including nonlinearities in Fourier magnitude and phase that can be associated with material index and film thickness.[2,17] Moreover, small discrepancies between theory and experiment show up more clearly in the frequency domain. In more detailed modeling, we attributed these discrepancies in part to various attributes of the Mirau objective, including the polarizing properties of the Inconel beam splitter. This is precisely what we are looking for as an outcome of the modeling—a means of evaluating system performance by comparing theory with experiment.

10. Conclusions

Our research shows that an incoherent superposition model accurately predicts the main features of the interference signal generated in a height-scanning interferometer, including effects related to both the illumination geometry and the range of source wavelengths. The computational efficiency of our Fourier approach facilitates complex numerical modeling, including field-dependent effects and system imperfections, at relatively high speed. This calculation provides insight into the key characteristics of the signal for various geometries and surface types, including thin-films structures.

Appendix A: Derivation of Equation (15)

In the text we derive the following expression for the Fourier components of a low-coherence interference signal [see Eq. (13)]:

$$q(K) = \int_0^{\infty}\int_0^{2k} \delta(K)(R+Z)\Gamma \mathrm{d}\hat{\kappa}\mathrm{d}k + \int_0^{\infty}\int_0^{2k} \delta(K-\hat{\kappa})\sqrt{RZ}\exp[i\hat{\kappa}h + i(\upsilon - \omega)]\Gamma \mathrm{d}\hat{\kappa}\mathrm{d}k + \int_0^{\infty}\int_0^{2k} \delta(K+\hat{\kappa})\sqrt{RZ} \times \exp[-i\hat{\kappa}h - i(\upsilon-\omega)]\Gamma \mathrm{d}\hat{\kappa}\mathrm{d}k. \quad \text{(A1)}$$

These integrals can be further simplified when we note the following properties of the product of a delta function δ with an arbitrary function $f(\hat{\kappa}, k)$ in a definite integral and use the Heaviside function to recast the integration limits:

$$\int_0^{2k} \delta(K) f(\hat{\kappa}, k)\mathrm{d}\hat{\kappa} = \delta(K)\int_0^{\infty} H(2k - \hat{\kappa}) f(\hat{\kappa}, k)\mathrm{d}\hat{\kappa}, \quad \text{(A2)}$$

$$\int_0^{2k} \delta(K-\hat{\kappa}) f(\hat{\kappa}, k)\mathrm{d}\hat{\kappa} = H(K) f(K, k) H(2k-K), \quad \text{(A3)}$$

$$\int_0^{2k} \delta(K+\hat{\kappa}) f(\hat{\kappa}, k)\mathrm{d}\hat{\kappa} = H(K) f(-K, k) H(2k+K). \quad \text{(A4)}$$

Using Eqs. (A2)–(A4), Eq. (13) becomes

$$q(K) = \delta(K)\int_0^{\infty}\int_0^{\infty} H(2k-\hat{\kappa})(R+Z)\Gamma \mathrm{d}\hat{\kappa}\mathrm{d}k + \int_0^{\infty} H(K)H(2k-K)\sqrt{RZ}\exp[i\hat{\kappa}h + i(\upsilon - \omega)]\Gamma \mathrm{d}k + \int_0^{\infty} H(K)H(2k+K)\sqrt{RZ} \times \exp[-i\hat{\kappa}h - i(\upsilon-\omega)]\Gamma \mathrm{d}k. \quad \text{(A5)}$$

Now using

$$\int_0^{\infty}\int_0^{\infty} H(2k-\hat{\kappa}) f(\hat{\kappa}, k)\mathrm{d}\hat{\kappa}\mathrm{d}k = \int_0^{\infty}\int_0^{\infty} H(2k-\hat{\kappa}) f(\hat{\kappa}, k)\mathrm{d}k\mathrm{d}\hat{\kappa}, \quad \text{(A6)}$$

$$\int_0^{\infty} H(K) f(K, k) H(2k-K)\mathrm{d}k = H(K)\int_{K/2}^{\infty} f(K, k)\mathrm{d}k, \quad \text{(A7)}$$

$$\int_0^{\infty} H(-K) f(-K, k) H(2k+K)\mathrm{d}k = H(-K)\int_{-k/2}^{\infty} f(-K, k)\mathrm{d}k, \quad \text{(A8)}$$

we have the desired result:

$$q(K) = \delta(K)\int_0^{\infty}\int_{\hat{\kappa}/2}^{\infty} (R+Z)\Gamma \mathrm{d}k\mathrm{d}\hat{\kappa} + H(K)\exp(iKh)\int_{K/2}^{\infty} \{\sqrt{RZ}\exp[i(\upsilon - \omega)]\Gamma\}_{\hat{\kappa}=+K}\mathrm{d}k + H(-K)\exp(-iKh) \times \int_{-K/2}^{\infty} \{\sqrt{RZ}\exp[-i(\upsilon-\omega)]\Gamma\}_{\hat{\kappa}=-K}\,\mathrm{d}k. \quad \text{(A9)}$$

The authors gratefully acknowledge the contributions of David Grigg, Jim Kramer, and Jim Biegen to this research.

References

1. H. Haneishi, "Signal processing for film thickness measurements by white light interferometry," Graduate thesis (Department of Communications and Systems Engineering, University of Electro-communications, Chofu, Tokyo, 1984).
2. P. de Groot, "Method and apparatus for surface topography measurement by spatial-frequency analysis of interferograms," U.S. patent 5,398,113 (14 March 1995).
3. T. Dresel, G. Häusler, and H. Venzke, "Three-dimensional sensing of rough surfaces by coherence radar," Appl. Opt. **31,** 919–925 (1992).
4. P. J. Caber, S. J. Martinek, and R. J. Niemann, "A new interferometric profiler for smooth and rough surfaces," in *Laser Dimensional Metrology: Recent Advances for Industrial Application*, M. J. Downs, ed., Proc. SPIE **2088,** 195–203 (1993).
5. J. Biegen, "Determination of the phase change on reflection from two-beam interference," Opt. Lett. **19,** 1690–1692 (1994).
6. M. Davidson, K. Kaufman, I. Mazor, and F. Cohen, "An application of interference microscopy to integrated circuit inspection and metrology," in *Integrated Circuit Metrology, Inspection, and Process Control*, K. M. Monahan, ed., Proc SPIE **775,** 233–247 (1987).
7. G. S. Kino and S. S. C. Chim, "Mirau correlation microscope," Appl. Opt. **29,** 3775–3783 (1990).
8. C. J. R. Sheppard and K. G. Larkin, "Effect of numerical aperture on interference fringe spacing," Appl. Opt. **34,** 4731–4733 (1995).
9. K. Nakano, H. Yoshida, K. Hane, S. Okuma, and T. Eguchi, "Fringe scannning interferometric imaging of small vibration using pulsed laser diode," Trans. SICE **31,** 454–460 (1995).
10. R. C. Gutierrez, K. V. Shcheglov, and T. K. Tang, "Pulsed-source interferometry for characterization of resonant micromachined structures," presented at the Solid-State Sensor and Actuator Workshop, Hilton Head Island, S.C., 8–11 June 1998.
11. M. Born and E. Wolf, *Principles of Optics*, 6th ed. (Pergamon, Oxford, UK, 1987), p. 40.
12. Ref. 11, p. 62.
13. P. A. Flournoy, R. W. McClure, and G. Wyntjes, "White-light interferometric thickness. gauge," Appl. Opt. **11,** 1907–1915 (1972).
14. A. Bosseboeuf and S. Petigrand, "Application of microscopic interferometry techniques in the MEMS field," in *Microsystems Engineering: Metrology and Inspection III*, C. Soreeki, ed., Proc. SPIE **5145,** 1–16 (2003).
15. P. de Groot and X. Colonna de Lega, "Signal modeling for modern interference microscopes," in *Optical Metrology in Production Engineering*, W. Osten and M. Takeda, eds., Proc. SPIE **5457,** 26–34 (2004).
16. A. Pförtner and J. Schwider, "White-light-interferometry suffering from dispersion deviations," Annual report (Lehrstuhl für Optik, University of Erlangen-Nürnberg, Berlin, 2000), p. 40.
17. S. W. Kim and G. H. Kim, "Method for measuring a thickness profile and a refractive index using white-light scanning interferometry and recording medium therefor," U.S. patent 6,545,763 (8 April 2003).